Environmental Science & Technology

Article

pubs.acs.org/est

Self-Protection Mechanism of Hexagonal WO_3–Based $DeNO_x$ Catalysts against Alkali Poisoning

Li Zheng,[†,§] Meijuan Zhou,[†,§] Zhiwei Huang,[†] Yaxin Chen,[†] Jiayi Gao,[†] Zhen Ma,[†] Jianmin Chen,[†] and Xingfu Tang*[,†,‡]

[†]Institute of Atmospheric Sciences, Shanghai Key Laboratory of Atmospheric Particle Pollution & Prevention (LAP^3), Department of Environmental Science & Engineering, Fudan University, Shanghai 200433, China

[‡]Jiangsu Collaborative Innovation Center of Atmospheric Environment and Equipment Technology (CICAEET), Nanjing University of Information Science & Technology, Nanjing 210044, China

Supporting Information

ABSTRACT: A good catalyst for efficiently controlling NO_x emissions often demands strong resistance against alkali poisoning. Although the traditional ion-exchange model, based on acid–base reactions of alkalis with Brønsted acid sites, has been established over the past two decades, it is difficult to be used as a guideline to develop such an alkali-resistant catalyst. Here we establish a self-protection mechanism of $DeNO_x$ catalysts against alkali poisoning by systematically studying the intrinsic nature of alkali resistance of V_2O_5/HWO (HWO = hexagonal WO_3) that shows excellent resistance to alkali poisoning in selective catalytic reduction of NO_x with NH_3 (SCR). Synchrotron X-ray diffraction and absorption spectroscopies demonstrate that V_2O_5/HWO has spatially separated catalytically active sites (CASs) and alkali-trapping sites (ATSs). During the SCR process, ATSs spontaneously trap alkali ions such as K^+, even if alkali ions initially block CASs, thus releasing CASs to realize the self-protection against alkali poisoning. X-ray photoelectron spectra coupled with theoretical calculations indicate that the electronic interaction between the alkali ions and ATSs with an energy saving is the driving force of the self-protection. This work provides a strategy to design alkali-resistant $DeNO_x$ catalysts.

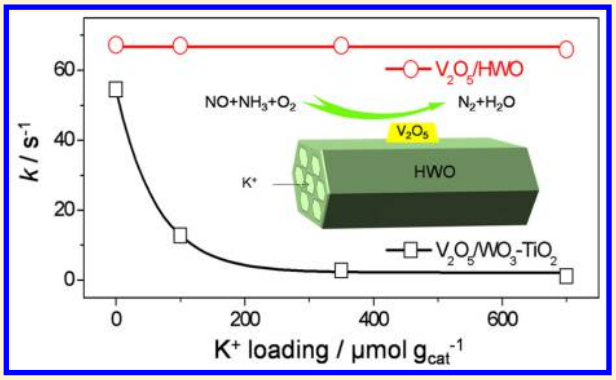

INTRODUCTION

Nitrogen oxides (NO_x) emitted from industrial glass and cement boilers, steel furnaces, and biofueled boilers have a great contribution to atmospheric pollution, especially in developing countries such as China.[1,2] Therefore, the related regulations for NO_x emissions control are increasingly stringent. Although selective catalytic reduction of NO_x by NH_3 (SCR) is one of the most promising technologies due to its high efficiency, commercial V_2O_5/TiO_2 catalysts promoted with WO_3 or MoO_3 suffer from severe deactivation due to the abundant alkali and alkaline earth metal ions contained in stack gases,[3−5] making it unfeasible to use commercial catalysts in these boilers/furnaces, especially in the presence of SO_2 in the stack gas.[6] Therefore, it is extremely desirable to develop strong alkali-resistant $DeNO_x$ catalysts.

Much effort has been made to design such $DeNO_x$ catalysts, and an ion-exchange model has also been proposed to account for the deactivation mechanism by alkalis.[3,4] This ion-exchange model is characteristic of a stoichiometric acid–base reaction of protons with alkali ions ($M{-}OH + A^+ \rightarrow M{-}O{-}A + H^+$, M = transition metal ions, A^+ = alkali metal ions).[3,4] According to this model, in order to develop alkali-resistant $DeNO_x$ catalysts, one can increase the amount of active components, use strong acidic supports, and/or select basic transition metal oxides as active components. For instance, Putluru et al.[7] supported "basic" CuO on acidic zeolites to get improved catalysts. Although alkali resistance was enhanced to some extent, the catalytic activity continuously decreased as more alkali ions accumulated. Since the ion-exchange model emphasizes the interaction between Brønsted acid sites and alkali ions only from the chemical kinetics point of view, $DeNO_x$ catalysts developed according to that model are still susceptible to deactivation by alkali ions.[8−12]

We recently established an exchange-coordination model to account for the alkali-resistant mechanism of a Hollandite $DeNO_x$ catalyst.[13] This model considers the interactions between alkalis and catalysts from both chemical kinetics and thermodynamics viewpoints: alkali ions first kinetically interact with catalysts' Brønsted acid sites through ion-exchange reactions; the exchanged alkali ions are thermodynamically stabilized via a coordination model to reach a steady state. This exchange-coordination model can serve as a criterion to guide the rational design of alkali-resistant $DeNO_x$ catalysts, and these catalysts such as hollandite manganese oxides[13,14] and CeO_2 supported on

Received: June 28, 2016
Revised: September 19, 2016
Accepted: September 30, 2016
Published: September 30, 2016

DOI: 10.1021/acs.est.6b03203
Environ. Sci. Technol. 2016, 50, 11951−11956

protonated titanate supports[15,16] often have specific alkali-trapping sites (ATSs) spatially separated from catalytically active sites (CASs).[14] Typically, a hexagonal WO_3 (HWO) with rich ATSs was used as a support to prepare V_2O_5/HWO catalysts with exceptional resistance to alkali poisoning in the SCR reactions in the presence of high-concentration SO_2 of 1300 mg m^{-3}, even if alkali ions initially blocked the CASs.[17] Therefore, deNO_x catalysts developed according to the exchange-coordination model can realize the self-protection against alkali poisoning during the SCR reactions.

In this work, we investigate the intrinsic nature of this mechanism in terms of the electronic interaction between alkalis and catalysts and establish a self-protection mechanism of V_2O_5/HWO catalysts against alkali poisoning. First, the alkali resistance of V_2O_5/HWO catalysts was studied by using in situ and ex situ alkali-trapping processes in the SCR reactions. Next, sophisticated synchrotron X-ray diffraction and absorption spectroscopies were used to precisely determine the accurate location of alkali ions (here K^+ ions are used as a typical representative of catalyst poisons) in the ATSs after trapping. Finally, X-ray photoelectron spectroscopy coupled with theoretical calculations reveals that the electronic interaction between alkali ion and the catalyst is the driving force for the self-protection of the catalysts against alkali poisoning.

EXPERIMENTAL SECTION

Materials Preparation. HWO was prepared by a hydrothermal method.[17] Briefly, an aqueous solution (80 mL) containing $(NH_4)_{10}W_{12}O_{41}$ (0.7 mmol), $(NH_4)_2SO_4$ (63.0 mmol), and oxalic acid (23.3 mmol) was charged into an autoclave (100 mL) and kept at 180 °C for 12 h with stirring. The slurry was then filtered, washed with deionized water, and dried at 105 °C for 12 h. V_2O_5/HWO was prepared by wet impregnation: HWO (2.000 g) was added to 15 mL of deionized water at 80 °C under magnetic stirring, to which 0.44 mmol NH_4VO_3 was added. The suspension was kept at 80 °C under stirring until dry, and the solid was dried at 105 °C for 12 h and calcined at 400 °C for 4 h. For comparison, a conventional V_2O_5/WO_3−TiO_2 catalyst containing 3.0 wt % V_2O_5 and 9.0 wt % WO_3 was prepared by impregnation.[17] To further load K^+, V_2O_5/HWO was impregnated with a K_2SO_4 solution. K_2SO_4−V_2O_5/HWO was obtained after being dried at 105 °C for 12 h and then calcined at 350 °C for 12 h to get V_2O_5/K_{in}HWO. The K^+ loading is expressed in terms of molar concentration of K^+ with respect to the weight of catalyst (μmol g_{cat}^{-1}).

Catalytic Evaluation. In situ and ex situ SCR reactions were performed in a fixed-bed quartz reactor (i.d. = 8 mm) under atmospheric pressure. A certain amount of catalyst (40−60 mesh) was charged for each run. The feed gas was composed of 1000 ppm of NO, 1000 ppm of NH_3, 3.0 vol % O_2, and balanced N_2, or He (when used). The total flow rate was 500 mL min^{-1}. Different gas hourly space velocities (GHSVs) were obtained by changing the volumes of catalysts. The concentrations of NO and NO_2 in the inlet and outlet gas were measured by an online chemiluminescence NO−NO_2−NO_x analyzer (42*i*-HL, Thermo Electron Corporation, U.S.A.), and the concentrations of N_2 and N_2O were detected by an online GC (Agilent 7890A) with a TCD detector for N_2 selectivity calculations (when used). For reaction kinetics, effects from external and internal diffusion were eliminated by varying the linear velocity of the feed gas passing through catalysts and the size of catalysts' particles, respectively, as confirmed in Figure S1.

Materials Characterization. Synchrotron X-ray diffraction (SXRD) patterns were performed at BL14B of the Shanghai Synchrotron Radiation Facility (SSRF) at a wavelength of 1.2398 Å. X-ray absorption spectra (XAS) at K *K*-edge of these samples were measured at BL4B7A of the Beijing Synchrotron Radiation Facility (BSRF) with the electron beam energy of 2.21 GeV and a ring current of 300−450 mA. Data analyses were conducted by using the IFEFFIT 1.2.11 software package. Transmission electron microscopy (TEM) and high-resolution TEM (HRTEM) images were obtained on a JEM 2100F transmission electron microscope. An FEI Tecnai G2 F20 S-Twin transmission electron microscope was used to perform scanning TEM (STEM) characterization with energy dispersive X-ray (EDX) mapping. The X-ray photoelectron spectra (XPS) were undertaken using Kratos Axis Ultra-DLD system with a charge neutralizer and a 150 W Al (Mono) X-ray gun (1486.6 eV) with a delay-line detector (DLD). The binding energies of the samples were calibrated according to the C 1s XPS at the binding energy of 284.6 eV. The curve fitting was carried out by using XPSPEAK 4.1 with a Shirley background.

Theoretical Calculations. Density functional theory (DFT) calculations were carried out using Vienna ab initio Simulation Package (VASP). A general gradient approximation (GGA) was employed for the description of exchange and correlation effects. We used the pseudo potentials of projector augmented wave method to describe the interactions between the core and valence electrons. The energy cutoff for the plane-waves was set to 450 eV. In the calculation of HWO, the lattice constant for a conventional hexagonal cell with space group of *P6/mmm* is 7.319 Å × 7.319 Å × 3.881 Å (Table S1). A 2 × 2 × 3 monkhorst-pack grid was used in the k-point sampling for the calculation. A supercell of 8 formula units of HWO was employed in the charge calculations of K^+ ions inside and outside the tunnels.

RESULTS AND DISCUSSION

The alkali resistance of V_2O_5/HWO was investigated by in situ and ex situ alkali trapping in the SCR process. To study the in situ alkali-trapping, we loaded K_2SO_4 (amount: 350 μmol g_{cat}^{-1}) on the surface of V_2O_5/HWO and dried the catalyst at 105 °C for 12 h, without further annealing at elevated temperatures. We then conducted two consecutive temperature-programmed SCR reactions and plotted the NO conversion (X_{NO}) as a function of reaction time in Figure 1a. In the first run, the X_{NO} increases as the reaction temperature increases from 100 to 350 °C at a ramping rate of 2 °C min^{-1} and arrives at a steady state with a ∼80% X_{NO} during the isothermal process at 350 °C. After that, the catalyst was cooled down to 100 °C, and then the second run was conducted. Obviously, the catalyst shows higher catalytic activity in the second run than in the first run, but in the isothermal process the X_{NO} at the steady state shows the same values of ∼80%.

The corresponding first derivative of the X_{NO} is shown in Figure 1b. The X_{NO} profiles can be classified into four stages: in the first stage (100−140 °C), the X_{NO} slightly increases with the reaction temperature in both runs, but for the first run the increment rate of the X_{NO} arrives at the first maximum at ∼140 °C. In the second stage (140−270 °C), the increment rate of the X_{NO} initially decreases slightly and then gradually increases in the first run, while the increment rate of the X_{NO} continuously increases and reaches a maximum at ∼270 °C for the second run. In the third stage, there are two completely different characteristics for both runs, i.e., the increment rate of the X_{NO} drastically increases in the first run and gradually decreases in the second

DOI: 10.1021/acs.est.6b03203
Environ. Sci. Technol. 2016, 50, 11951−11956

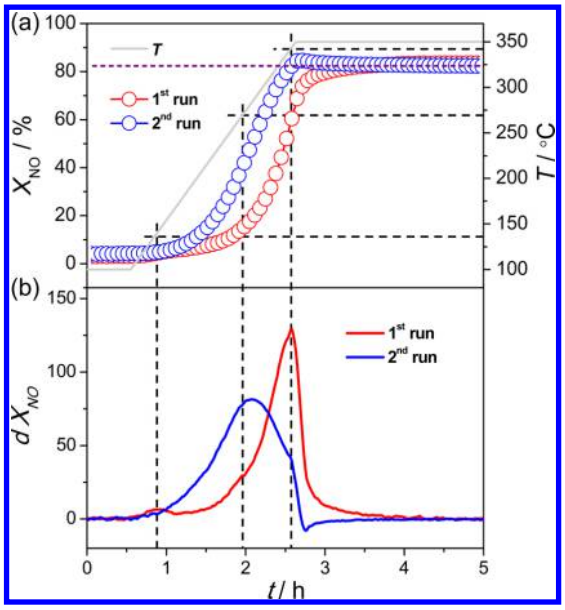

Figure 1. In situ alkali-trapping process over V_2O_5/HWO with a K^+ loading of 350 μmol g_{cat}^{-1} during SCR. (a) X_{NO} with time on stream in two consecutive runs at a ramping rate of 2 °C min^{-1}. After the first run, the catalyst was cooled to 100 °C (T represents reaction temperature). Reaction conditions: 1000 ppm of NO, 1000 ppm of NH_3, 3.0 vol % O_2, balance N_2, and GHSV 80 000 h^{-1}. (b) The corresponding first derivative of X_{NO} as a function of time (t).

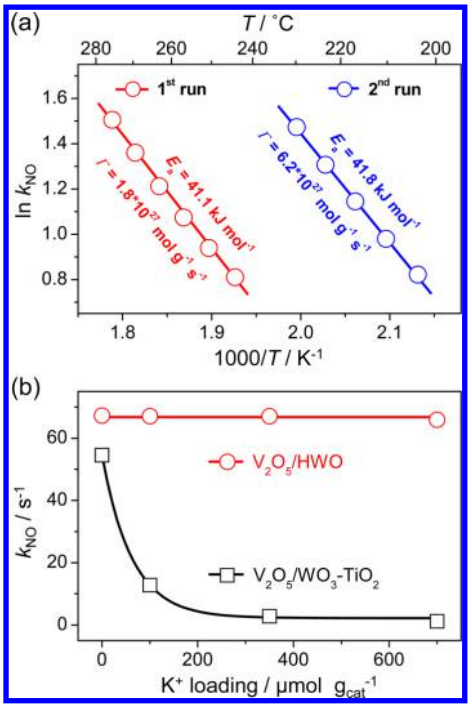

Figure 2. (a) Arrhenius plot for two runs with the pre-exponential factors (Γ) and activation energy (E_a) of SCR. (b) The k_{NO} as a function of K^+ loading on V_2O_5/HWO and V_2O_5/WO_3−TiO_2. The catalysts were annealed at 350 °C after K_2SO_4 loading. Catalytic tests were conducted at 350 °C. Reaction conditions: 1000 ppm of NO, 1000 ppm of NH_3, 3.0 vol % O_2, balance N_2, and GHSV 40 000 h^{-1}.

run. In the fourth stage (270−350 °C, including the isothermal process at 350 °C), both runs bear similar characteristics, and the increment rates of the X_{NO} in both runs decrease drastically down to zero.

In view of the low Hütigg temperature of K_2SO_4 ($T_{Hüt}$ = 130 °C),[18] the X_{NO} of the second stage (140−270 °C) of the first run is much lower than that of the second run, probably because the diffusion of K^+ on the surface of V_2O_5/HWO leads to the blockage of some catalytically active sites (CASs). In the third stage of the first run, the incremental rate of the X_{NO} rapidly increases, certainly due to the release of CASs caused by the migration of K^+ ions into the HWO tunnels. At ∼ 270 °C, all the K^+ ions are captured in the HWO tunnels and all the CASs are exposed, and thus in the fourth stage of the first run, the catalyst shows high catalytic activity, similar to that observed in the fourth stage of the second run. Furthermore, the conversion curve in the second run shows identical characteristics as the conversion curve obtained by using K^+-free V_2O_5/HWO (Figure S2), implying that all the CASs are released due to the migration of K^+ in the HWO tunnels. Two consecutive runs with the same procedure were also conducted to comparatively study the alkali-resistant ability of V_2O_5/WO_3−TiO_2 in the SCR process (Figure S3). Obviously, K^+ covered the surfaces and blocked the catalytically active sites of V_2O_5/WO_3−TiO_2 after the thermal diffusion in the first run, and complete deactivation occurred judging from the extremely low X_{NO} value in the second run.

In order to shed light on the difference between the two runs above and alkali resistance of the catalyst, reaction kinetics and ex situ alkali-trapping process in SCR were studied (Figure 2). The X_{NO} is controlled to be lower than 20% for both runs, and the corresponding Arrhenius curves are given in Figure 2a. The apparent activation energy (E_a) over V_2O_5/HWO in the first run is ∼41 kJ mol^{-1}, which is almost the same as that (∼42 kJ mol^{-1}) in the second run, implying that the natures of CASs in both runs are identical to each other. To differentiate the catalytic performance between two runs, their pre-exponential factors (Γ) of the reactions were calculated according to the Arrhenius eq (Figure 2a). The Γ in the second run is ∼6.2 × 10^{27} molecules g_{cat}^{-1} s^{-1}, three times larger than the corresponding value in the first run (∼1.8 × 10^{27} molecules g_{cat}^{-1} s^{-1}), implying that the number of CASs in the second run is much larger than that in the first run. Our data demonstrate that the CASs, initially blocked by surface K^+ ions, are released after the first run due to the migration of K^+ ions into the HWO tunnels at high reaction temperatures.[14,17]

We additionally conducted ex situ alkali-trapping experiments by pretreating V_2O_5/HWO with different K_2SO_4 loadings at 350 °C. For comparison, a conventional V_2O_5/WO_3−TiO_2 catalyst was also loaded with the same K_2SO_4 loadings and annealed at 350 °C for SCR tests. Figure 2b shows the NO reaction rate (k_{NO}) of the catalysts with different alkali loadings at 350 °C. V_2O_5/HWO shows excellent alkali resistance even at a high alkali loading of 700 μmol g_{cat}^{-1}. The catalyst gives the same k_{NO} at 350 °C, regardless of the alkali loading. In contrast, V_2O_5/WO_3−TiO_2 exhibits rather poor alkali resistance. The catalyst undergoes severe deactivation even at a low K^+ loading (100 μmol g_{cat}^{-1}), and it is completely deactivated as the K^+ loading reaches ∼200 μmol g_{cat}^{-1}. Note that V_2O_5/HWO has not only the extraordinary alkali-resistant ability but also excellent water tolerance (Figure S4) and high selectivity to N_2 (Figure S5), which allows it to be used under real SCR conditions in the coexistence of alkalis and water.

To investigate the position of K^+ in V_2O_5/HWO after the in situ or ex situ SCR reactions above, we collected the SXRD patterns of V_2O_5/HWO, K_2SO_4−V_2O_5/HWO, and V_2O_5/K_{in}HWO (Figure S6), where K_2SO_4−V_2O_5/HWO and V_2O_5/K_{in}HWO represent V_2O_5/HWO with the K_2SO_4 loading before

DOI: 10.1021/acs.est.6b03203
Environ. Sci. Technol. 2016, 50, 11951−11956

and after the ex situ alkali-trapping process, respectively, and K_{in}HWO stands for HWO full of K^+ ions in the tunnels. Owing to the low V_2O_5 loading (1 wt % with respect to V_2O_5/HWO) and its high dispersion on the surfaces, main diffractions can be indexed to HWO with a hexagonal structure of a space group *P6/mmm*.[17] No reflections attributed to K_2SO_4, K_2CO_3, or K_2O can be distinguished, indicating that K^+ species disperse highly on the surface. The STEM image of V_2O_5/K_{in}HWO, the corresponding EDX mappings, and EDX analysis (Figure S7) demonstrate the high dispersion of K^+ species.[17]

To precisely determine the position of K^+ in V_2O_5/K_{in}HWO, we conducted Rietveld refinement analyses of the SXRD patterns and the XAS at the K *K*-edge of the samples. Rietveld refinement analyses gave a coordination configuration of WO_6 polyhedron and lattice parameters (Tables S1, S2). HWO is constructed by corner-sharing WO_6 octahedra, and there are hexagonal tunnels oriented along the *c* axis with the size of ~5.4 Å, and many metal ions including alkali ions can readily insert into the tunnels by ion-exchange.[19,20] Figure 3 shows the SXRD pattern of V_2O_5/K_{in}HWO, and the hexagonal structure of HWO in V_2O_5/K_{in}HWO with the space group *P6/mmm* is preserved after the ex situ K^+-trapping process (Tables S1, S2). After the Rietveld refinement, the K^+ location can be assigned to be at the Wyckoff 1*a* site or the (0,0,0) site,[17] and the trapped K^+ is located at the center of a plane consisting of six tunnel oxygen ions, as shown in the inset of Figure 3, and the length of the K−O bond is estimated to be ~2.66 Å. Hence, as calculated, HWO with a "single-walled" subnanometer tunnel structure has a high capacity of ~720 μmol g_{cat}^{-1} (Supporting Information).

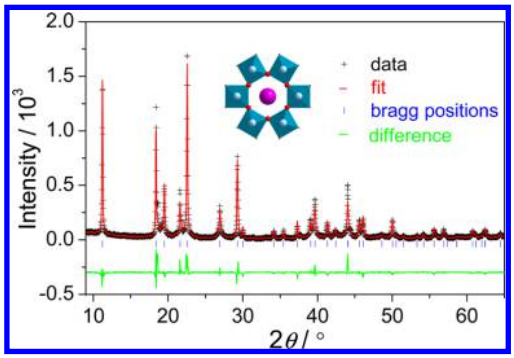

Figure 3. SXRD pattern of V_2O_5/K_{in}HWO. The green curve is the differential SXRD pattern. The short vertical lines below the SXRD pattern mark the peak positions of all the possible Bragg reflections. Inset: Model showing the K^+ position located in the HWO tunnel. Red, blue, and purple balls represent O, W, and K atoms, respectively, and the blue octahedron does the WO_6 motif.

Extended X-ray absorption fine structure (EXAFS) spectroscopy was used to determine the local structures of K^+ in the tunnels of V_2O_5/K_{in}HWO. Figure 4 shows the Fourier transform (FT) amplitudes of the EXAFS spectra of V_2O_5/K_{in}HWO and a reference K_2SO_4 with k^2 weight at the K *K*-edge, and the spectra of V_2O_5/K_{in}HWO with different k^n weights (n = 1, 2, or 3) are also plotted in Figure 4 in order to precisely identify the immediate environment of K^+. Some structural parameters obtained by fitting the spectra with theoretical models are listed in Table S3,[17] and curve-fitting of *R*-space and inverse FT spectra are given in Figure S8. Obviously, V_2O_5/K_{in}HWO gives significantly different local environments of K^+ from those in K_2SO_4. The first shell of the spectra of V_2O_5/K_{in}HWO can be ascribed to the K−O bonds with a bond length of ~2.64 Å and a

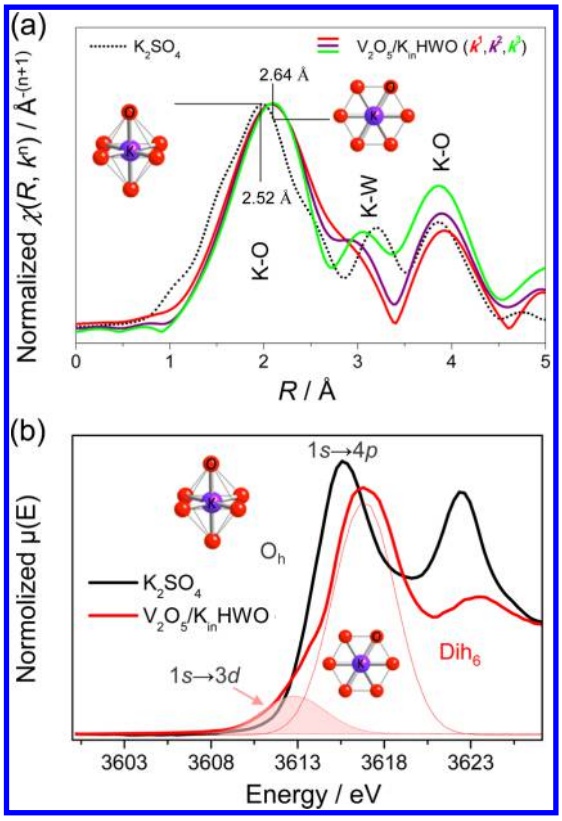

Figure 4. (a) FT EXAFS spectra of V_2O_5/K_{in}HWO with different k^n weight (n = 1, 2, or 3) and K_2SO_4 with k^2 weight at the K *K*-edge. (b) XANES spectra of V_2O_5/K_{in}HWO and K_2SO_4 together with spectral fitting edges of the pre-edge XANES spectra of V_2O_5/K_{in}HWO. A red shade represent a dipole-allowed 1s → 3d transition. Inset structural models: a planar KO_6 coordination configuration with a Dih_6 symmetry in V_2O_5/K_{in}HWO and a KO_6 octahedron with an O_h symmetry in K_2SO_4. The purple and red balls represent K and O atoms, respectively.

coordination number (CN) of 6, consistent with the above SXRD pattern, as modeled in the inset of Figure 4. The second shell is assigned to the near neighbor K−W interatomic distance according to the different amplitudes with different *k* weights (Table S3). The first strong amplitude in the FT spectra of K_2SO_4 is attributed to the K−O bonds with an average bond length of ~2.52 Å and a CN of 6, consistent with a KO_6 octahedron with an O_h symmetry in the K_2SO_4 crystal structure,[21] also shown in the inset of Figure 4b.

Since the pre-edge features of X-ray absorption near edge structure (XANES) spectra are sensitive to the coordination geometry of excited atoms,[20] we collected the XANES spectra of V_2O_5/K_{in}HWO and K_2SO_4 at the K *K*-edge. In Figure 4b, the first absorption peaks in the pre-edge feature for V_2O_5/K_{in}HWO and K_2SO_4 demonstrate significant difference.[22,23] A strong absorption feature at the K *K* pre-edge of V_2O_5/K_{in}HWO is attributed to the dipole-allowed 1s → 3d transition (the red shade in Figure 4b), while no strong intensity pre-edge is observed for K_2SO_4 due to the dipole-forbidden transition for the centro-symmetric octahedral K centers. This indicates that the coordination geometry of K centers in V_2O_5/K_{in}HWO is different from that in K_2SO_4, consistent with the SXRD data above that the K^+ ions in V_2O_5/K_{in}HWO and K_2SO_4 have the planar KO_6 configuration with a Dih_6 symmetry and a octahedral KO_6 geometry, respectively.[20] A combination of the EXAFS and XANES spectra with the Rietveld refinement analysis of the

DOI: 10.1021/acs.est.6b03203
Environ. Sci. Technol. 2016, 50, 11951−11956

SXRD patterns demonstrates that the K^+ ions of $V_2O_5/K_{in}HWO$ are trapped in the HWO tunnels and located at the Wyckoff 1*a* sites or the (0,0,0) sites (Figure 4 and Tables S1, S2).

To better understand the nature of the alkali-resistant mechanism of V_2O_5/HWO, we investigated the electronic states by conducting XPS measurements and DFT calculations. The K 2p XPS of $V_2O_5/K_{in}HWO$ and K_2SO_4 are shown in Figure 5a.

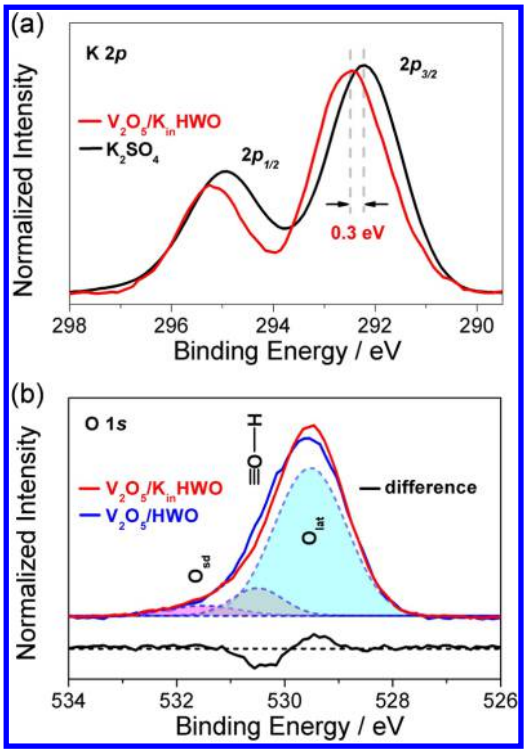

Figure 5. (a) K 2p XPS of $V_2O_5/K_{in}HWO$ and K_2SO_4. (b) O 1s XPS of $V_2O_5/K_{in}HWO$ and V_2O_5/HWO together with their difference. The shades in different colors show curve-fitting results, and the shades in pink, gray, and light blue represent surface defect O (O_{sd}), tunnel lattice O connected with protons (≡O−H), and surface lattice O (O_{lat}) species, respectively.

The K 2p core-level binding energy of $V_2O_5/K_{in}HWO$ is centered at ~292.6 eV, and it shifts up by 0.3 eV compared with that of K_2SO_4 (~292.3 eV). This indicates that part of the electrons of K transfer to HWO after the ion-exchange reactions between the HWO tunnel protons and K^+ in K_2SO_4, in accordance with the partially unoccupied frontier orbitals of K after being trapped in the HWO tunnels, as shown in the related XANES spectrum of Figure 4b. For potassium atoms with the outmost electron structure of $3p^64s^13d^0$ at the ground states, the oxidation state that approaches +1 is more stable due to the relatively stable electronic configuration than metallic potassium atoms. Hence, K^+ becomes more stable after being trapped by six oxygen atoms on the walls of the HWO tunnels.[17]

Figure 5b depicts the O 1s XPS of $V_2O_5/K_{in}HWO$ and V_2O_5/HWO together with their difference. A small difference is discernible in the O 1s spectra. In particular, the O 1s XPS of $V_2O_5/K_{in}HWO$ decreases in the binding energy range of 530−531 eV but increases around the binding energy of 529.5 eV, implying that the electron density of the lattice oxygen in $V_2O_5/K_{in}HWO$ increases after the trapping of K^+ in HWO tunnels. A combination of the electron characteristics of K ions and O ions demonstrates that the electron transfer occurs from K to O in $V_2O_5/K_{in}HWO$ because the oxidation states of tungsten and vanadium species are almost preserved after the alkali trapping according to the W 4f and V 2p XPS (Figures S9, S10). Thus, the electron transfer between alkalis and HWO leads to a more stable $K_{in}HWO$ structure than that of a system containing the surface K on HWO surfaces.

We further conducted DFT calculations to investigate the electronic interaction between K^+ and HWO. As shown in Figure 6, the isosurface of charge density difference of the planar KO_6

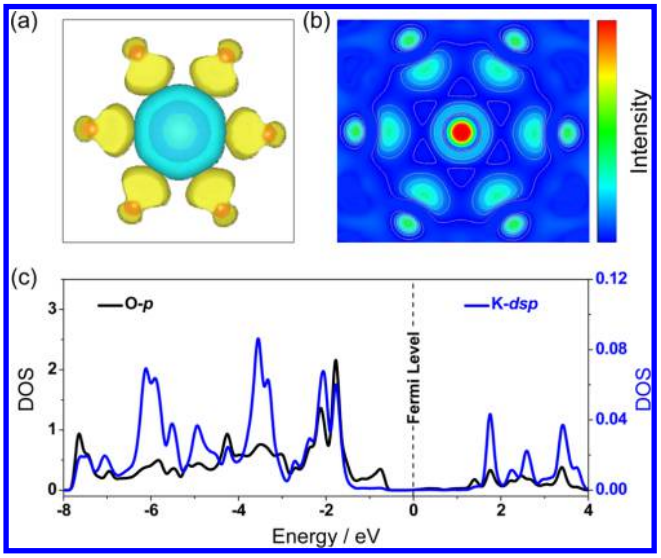

Figure 6. (a) Difference of the isosurface electronic density of the KO_6 structure motif. Electron depletion and accumulation are marked by cyan and yellow areas, respectively. (b) The contour electronic density difference of the KO_6 structure motif. (c) The DOS of the K dsp orbitals and the O p orbitals in $K_{in}HWO$.

structure motif demonstrates the strong electronic interaction between K^+ and O^{2-} occurs, which is closely asscoiated with the K^+ frontier dsp orbitals,[24−26] as confirmed by using the related K *K*-edge XANES spectra above (Figure 4b). Figure 6b illustrates the contour plot of the charge density difference of the planar KO_6 structure. The electronic density of six oxygen atoms in KO_6 increases along the direction pointing to the central K atom, indicating the presence of the electronic interaction between them, which results from the electron transfer from potassium to oxygen, consistent with the O 1s XPS in Figure 4b. The density of states (DOS) of the s, p, and d orbitals of the potassium of the planar KO_6 structure appears at the same energy regime, demonstrating the existence of dsp hybridization (Figure S11),[24−26] favorable for bonding to the O 2p orbitals, as shown in Figure 6c. As a consequence, the hybridization of the K dsp orbitals strengthens the K−O bonds with an energy saving of ~2.3 eV with respect to K^+ on the surface of HWO,[17] thus stabilizing the K^+ ions in the HWO tunnels. Therefore, the strong electronic interaction is the driving force of the extraordinary resistance of V_2O_5/HWO against alkali poisoning.

In conclusion, we established the self-protection mechanism of the V_2O_5/HWO catalyst against alkali poisoning in the SCR reactions. The combination of reaction kinetics with numerous characterization techniques such as SXRD patterns and X-ray absorption spectra demonstrated that K^+ ions spontaneously migrated from the CASs to the ATSs to realize the self-protection against alkali poisoning in the SCR reaction. The electronic interaction between K^+ and O^{2-} of HWO with an energy saving, according to the XPS and theoretical calculations, is the driving

DOI: 10.1021/acs.est.6b03203
Environ. Sci. Technol. 2016, 50, 11951−11956

force of the self-protection mechanism. The self-protection model assists the design of alkali-resistant deNO$_x$ catalysts to be used in industrial boilers with abundant alkali stack gases.

■ ASSOCIATED CONTENT

Supporting Information

The Supporting Information is available free of charge on the ACS Publications website at DOI: 10.1021/acs.est.6b03203.

Some related tables and figures (PDF)

■ AUTHOR INFORMATION

Corresponding Author

*Tel.: +86-21-65642997; fax: +86-21-65643597; e-mail: tangxf@fudan.edu.cn.

Author Contributions

§These authors contributed equally to this work.

Notes

The authors declare no competing financial interest.

■ ACKNOWLEDGMENTS

This work was financially supported by the NSFC (21277032 and 21477023) and the STCSM (14JC1400400). The SXRD and XAS measurements were conducted at the SSRF and BSRF, respectively. We acknowledge Pingping Hu, Junxiao Chen, and Zichenxi Dong from Fudan University for their assistance with the HWO preparation and valuable discussion.

■ REFERENCES

(1) Xiong, T.; Jiang, W.; Gao, W. Current status and prediction of major atmospheric emissions from coal-fired power plants in Shandong Province, China. *Atmos. Environ.* **2016**, *124*, 46−52.

(2) Hua, S.; Tian, H.; Wang, K.; Zhu, C.; Gao, J.; Ma, Y.; Xue, Y.; Wang, Y.; Duan, S.; Zhou, J. Atmospheric emission inventory of hazardous air pollutants from China's cement plants: Temporal trends, spatial variation characteristics and scenario projections. *Atmos. Environ.* **2016**, *128*, 1−9.

(3) Chen, J.; Yang, R. T. Mechanism of poisoning of the V_2O_5/TiO_2 catalyst for the reduction of NO by NH_3. *J. Catal.* **1990**, *125*, 411−420.

(4) Zheng, Y.; Jensen, A. D.; Johnsson, J. E. Laboratory investigation of selective catalytic reduction catalysts: Deactivation by potassium compounds and catalyst regeneration. *Ind. Eng. Chem. Res.* **2004**, *43*, 941−947.

(5) Kamata, H.; Takahashi, K.; Odenbrand, C. U. I. The role of K_2O in the selective reduction of NO with NH_3 over a $V_2O_5(WO_3)/TiO_2$ commercial selective catalytic reduction catalyst. *J. Mol. Catal. A: Chem.* **1999**, *139*, 189−198.

(6) Li, Q.; Chen, S.; Liu, Z.; Liu, Q. Combined effect of KCl and SO_2 on the selective catalytic reduction of NO by NH_3 over V_2O_5/TiO_2 catalyst. *Appl. Catal., B* **2015**, *164*, 475−482.

(7) Putluru, S. S. R.; Riisager, A.; Fehrmann, R. Alkali resistant Cu/zeolite deNO$_x$ catalysts for flue gas cleaning in biomass fired applications. *Appl. Catal., B* **2011**, *101* (3−4), 183−188.

(8) Putluru, S. S. R.; Jensen, A. D.; Riisager, A.; Fehrmann, R. Alkali resistant Fe-zeolite catalysts for SCR of NO with NH_3 in flue gases. *Top. Catal.* **2011**, *54* (16−18), 1286−1292.

(9) Li, F.; Zhang, Y.; Xiao, D.; Wang, D.; Pan, X.; Yang, X. Hydrothermal method prepared Ce−P−O catalyst for the selective catalytic reduction of NO with NH_3 in a broad temperature range. *ChemCatChem* **2010**, *2* (11), 1416−1419.

(10) Kustov, A. L.; Rasmussen, S. B.; Fehrmann, R.; Simonsen, P. Activity and deactivation of sulphated TiO_2- and ZrO_2-based V, Cu, and Fe oxide catalysts for NO abatement in alkali containing flue gases. *Appl. Catal., B* **2007**, *76* (1−2), 9−14.

(11) Busca, G.; Lietti, L.; Ramis, G.; Berti, F. Chemical and mechanistic aspects of the selective catalytic reduction of NO$_x$ by ammonia over oxide catalysts: A review. *Appl. Catal., B* **1998**, *18* (1−2), 1−36.

(12) Due-Hansen, J.; Boghosian, S.; Kustov, A.; Fristrup, P.; Tsilomelekis, G.; Ståhl, K.; Christensen, C. H.; Fehrmann, R. Vanadia-based SCR catalysts supported on tungstated and sulfated zirconia: Influence of doping with potassium. *J. Catal.* **2007**, *251* (2), 459−473.

(13) Hu, P.; Huang, Z.; Gu, X.; Xu, F.; Gao, J.; Wang, Y.; Chen, Y.; Tang, X. Alkali-resistant mechanism of a hollandite deNO$_x$ catalyst. *Environ. Sci. Technol.* **2015**, *49*, 7042−7047.

(14) Huang, Z.; Gu, X.; Wen, W.; Hu, P.; Makkee, M.; Lin, H.; Kapteijn, F.; Tang, X. A "smart" hollandite deNO$_x$ catalyst: Self-protection against alkali poisoning. *Angew. Chem., Int. Ed.* **2013**, *52*, 660−664.

(15) Chen, X.; Wang, H.; Wu, Z.; Liu, Y.; Weng, X. Novel $H_2Ti_{12}O_{25}$-confined CeO_2 catalyst with remarkable resistance to alkali poisoning based on the "shell protection effect". *J. Phys. Chem. C* **2011**, *115* (35), 17479−17484.

(16) Wang, P.; Wang, H.; Chen, X.; Liu, Y.; Weng, X.; Wu, Z. Novel SCR catalyst with superior alkaline resistance performance: Enhanced self-protection originated from modifying protonated titanate nanotubes. *J. Mater. Chem. A* **2015**, *3*, 680−690.

(17) Huang, Z.; Li, H.; Gao, J.; Gu, X.; Zheng, L.; Hu, P.; Xin, Y.; Chen, J.; Chen, Y.; Zhang, Z.; Chen, J.; Tang, X. Alkali- and sulfur-resistant tungsten-based catalysts for NO$_x$ emissions control. *Environ. Sci. Technol.* **2015**, *49* (24), 14460−14465.

(18) Moulijn, J. A.; van Diepen, A. E.; Kapteijn, F. Catalyst deactivation: Is it predictable? What to do? *Appl. Catal., A* **2001**, *212*, 3−16.

(19) Griffith, C. S.; Luca, V. Ion-exchange properties of microporous tungstates. *Chem. Mater.* **2004**, *16*, 4992−4999.

(20) Michailovski, A.; Kiebach, R.; Bensch, W.; Grunwaldt, J. D.; Baiker, A.; Komarneni, S.; Patzke, G. R. Morphological and kinetic studies on hexagonal tungstates. *Chem. Mater.* **2007**, *19*, 185−197.

(21) Bredig, M. A. Isomorphism and allotropy in compounds of the type A_2XO_4. *J. Phys. Chem.* **1942**, *46*, 747−764.

(22) Jürgensen, A. X-ray absorption spectroscopy of aqueous solutions in the X-ray energy region from 1800 to 3700 eV. *Can. J. Chem.* **2009**, *87*, 601−611.

(23) Tsai, H. M.; Asokan, K.; Pao, C. W.; Chiou, J. W.; Du, C. H.; Pong, W. F.; Tsai, M.-H.; Jang, L. Y. Anisotropic electronic structure in quasi-one-dimensional $K_{0.3}MoO_3$: An angle-dependent X-ray absorption study. *Appl. Phys. Lett.* **2007**, *91*, 022109.

(24) Xu, F.; Huang, Z. W.; Hu, P. P.; Chen, Y. X.; Zheng, L.; Gao, J. Y.; Tang, X. F. The promotion effect of isolated potassium atoms with hybridized orbitals in catalytic oxidation. *Chem. Commun.* **2015**, *51*, 9888−9891.

(25) Bordiga, S.; Groppo, E.; Agostini, G.; van Bokhoven, J. A.; Lamberti, C. Reactivity of surface species in heterogeneous catalysts probed by in situ X-ray absorption techniques. *Chem. Rev.* **2013**, *113*, 1736−1850.

(26) Pauling, L. *General Chemistry*; BN Publishing, 2011.

DOI: 10.1021/acs.est.6b03203
Environ. Sci. Technol. 2016, 50, 11951−11956